Benefits of stochastic weight averaging in developing neural network radiation scheme for numerical weather prediction

Hwan-Jin Song[1], Soonyoung Roh[1], Juho Lee[2], Giung Nam[2], Eunggu Yun[2], Jongmin Yoon[2], and Park Sa Kim[1]

[1]National Institute of Meteorological Sciences, Korea Meteorological Administration, Jeju-do, Republic of Korea

[2]Graduate School of Artificial Intelligence, Korea Advanced Institute of Science and Technology, Daejeon, Republic of Korea

Key Points

- The performance of the neural network radiation scheme was evaluated under a framework of ideal and real cases.

- Stochastic weight averaging is advantageous in generalization compared to the traditional neural network.

- Long-term forecast errors can be largely improved using stochastic weight averaging.

* Corresponding author's address
Hwan-Jin Song
National Institute of Meteorological Sciences,
63568, Seogwipo-si, Jeju-do, Republic of Korea
E-mail: hwanjinsong@gmail.com

34   **Abstract**

35   Stochastic weight averaging (SWA) was applied to improve the radiation emulator based on a

36   sequential neural network (SNN) in a numerical weather prediction model over Korea. While

37   the SWA has advantages in terms of generalization such as the ensemble model, the

38   computational cost is maintained at the same level as that of a single model. The

39   performances of both emulators were evaluated under ideal and real case frameworks.

40   Various sensitivity experiments using different sampling ratios, activation functions, hidden

41   layers, and batch sizes were also conducted. The emulators showed a 60-fold speedup for the

42   radiation processes and 84–87% reduction of the total computation. In the ideal simulation,

43   compared to the infrequent radiation scheme by 60 times, SNN improved forecast errors by

44   5.8–14.1%, and SWA further increased these improvements by 18.2–26.9%. In the real case

45   simulation, SNN showed 8.8% and 4.7% improvements for longwave and shortwave fluxes

46   compared to the infrequent method; however, these improvements deceased significantly

47   after 5 days, resulting in 1.8% larger error for skin temperature. By contrast, SWA showed

48   stable one-week forecast features with 12.6%, 8.0%, and 4.4% improvements in longwave

49   and shortwave fluxes, and skin temperature, respectively. Although the use of two hidden

50   layers showed the best performance in this study, it was thought that the optimal number of

51   hidden layers could differ depending on the given problem. Compared to temperature and

52   precipitation observations, all experiments showed a variability of error within 1%, implying

53   that the operational use of the developed emulators is possible.

54   **Keywords:** neural network, stochastic weight averaging, emulator, speedup, WRF, RRTMG

55

56

Plain Language Summary

The NN emulators for radiation parameterization were developed to accelerate the computational speed of the numerical weather forecasting model. Although previous studies have demonstrated that the computational speed for radiation processes can be improved tens of times, guaranteeing stability in long-term forecasting has been recognized as imperative for the operational use of radiation emulator. In general, the multi-model ensemble approach is used to reduce the uncertainty of a single model. However, this approach induces a significant computation burden in proportion to ensemble members. The alternative method developed in this study uses a stochastic averaging technique for weight coefficients during the NN training process, allowing processing to be conducted at the same computational cost as the single model because the dimensions of the final weights are maintained. Application of the trained NN emulator to the numerical model has demonstrated the advantages of generalization in various test cases, while exhibiting significant improvements in accuracy in the latter part of the forecast. This method can therefore contribute to improving emulator studies that face problems related to generalization.

1. Introduction

Longwave (LW) and shortwave (SW) radiation physics are important for describing the exchange of energy between the Earth and the Sun. Radiation is a fundamental energy source that determines large-scale atmospheric circulation and consequent physical processes. Accurate calculation involving radiation physics using the line-by-line model (Clough et al., 1992; 2005) requires high computational burden, rendering it important to develop methods that allow rapid calculation of the radiation process. The recent rapid advances in machine learning techniques has led to the development of neural network (NN) emulators for radiation processes in the two main fields: the radiative transfer model (RTM) and radiation parameterization for numerical weather–climate model. An NN emulator that can be used in the RTM was developed some time ago (Chevallier et al., 1998) and was applied to the data assimilation system of the numerical weather prediction (NWP) model (Chevallier et al., 2000). Recent RTM studies based on clear sky simulations have shown a of 1.87–10.88-fold speedup (Liu et al., 2020) when used with the Rapid Radiative Transfer Model for GCMs (RRTMG; Iacono et al., 2008), and 1.8–3.5-fold (Ukkonen et al., 2020) and up to 4-fold (Veerman et al., 2021) for the RRTMGP scheme (Iacono et al., 2008; Pincus et al., 2019). Note that the results of Liu et al. (2020) should be interpreted differently because the measurements described were obtained under different parallelization conditions. Meanwhile, Meyer et al. (2021) showed that using an emulator to add 3D cloud radiative effects was less than 1% more expensive than the 1D scheme; this was a significant decrease in computational cost because the 3D scheme was usually five-times as expensive than the 1D scheme. These results demonstrate the effectiveness of emulating cloud processes in terms of computational cost.

It is difficult to develop an emulator for radiation parameterization within the global circulation model (GCM) and NWP because of complex interactions with various processes

98   within numerical models. However, the emulator for numerical models is more valuable

99   because it can provide important forecasting information that includes factors such as climate

100   change and rapid floods. Thus, the reduction in computational cost associated with the

101   development of an emulator for use with the numerical model would be advantageous in

102   many ways (such as producing national policy or saving lives). Krasnopolsky et al. (2010)

103   used a GCM model of the National Oceanic and Atmospheric Administration (NOAA) with

104   coarse horizontal (~ 100 km) and temporal resolutions, to show that the NN emulator can

105   improve the computational speed of the RRTMG radiation processes by approximately 30

106   times (an average of LW and SW) and reduce 20–25% computational cost for the total model.

107   Notably, the total reduction calculated can vary with the computational percentage used for

108   the radiation scheme to that used for the total model. The deep neural network (DNN)

109   emulator that was developed by Pal et al. (2019) showed 8–10 times speedup for radiation

110   parameterization; however, the total reduction achieved in terms of computational cost was

111   not elucidated. Song and Roh (2021), and Song et al. (2021) performed NWP studies with 5-

112   km spatial and 20-s temporal resolution from the Korea Meteorological Administration

113   (KMA) to show a 60-fold speedup in RRTMG-K radiation parameterization (Iacono et al.,

114   2008; Beak, 2017), with an 87% reduction in the time taken for total model computation. The

115   significant difference in the total computation reduction achieved in GCM and NWP studies

116   is because GCMs typically use an hourly scale radiation time step (radt), whereas the NWP

117   studies used the same time step for both the total model and the radiation process (i.e., 20 s),

118   leading to a more accurate result but a higher computational burden for the control run (i.e.,

119   more speedup for the emulator).

120   All these studies of radiation emulators have mainly been developed using the NN or

121   DNN techniques because these methods can be simply implemented into Fortran in both the

122   GCM and NWP. However, recent developments have been made in machine learning

123   techniques based on the Python code. Ott et al. (2020) recently developed the Fortran-Keras

124   Bridge to communicate between Fortran and Python, and it is actively used in emulator

125   studies. However, such efforts remain within the scope of the DNN, and other deep learning

126   techniques have not yet been attempted. Although Liu et al. (2020) applied a convolutional

127   neural network (CNN) to a single column model, it was based on the use of a Python wrapper

128   outside the numerical model. For real-case modeling such as the GCM or NWP, which are

129   based on large-scale Fortran codes, this approach is difficult to apply. Most NN emulators for

130   radiation parameterization in the GCM and NWP have been developed by the NOAA

131   (Krasnopolsky et al., 2005, 2008, 2010; Belochitski et al., 2011; Belochitski and

132   Krasnopolsky, 2021) or the KMA (Roh and Song, 2020; Song and Roh, 2021; Song et al.,

133   2021) using Fortran software (Krasnopolsky, 2014). However, this software does not support

134   other activation functions other than tangent hyperbolic (Tanh), DNN with multiple hidden

135   layers, and batch (or parallel) learning. Although functions other than Tanh (e.g., sigmoid,

136   softsign, arctan, and rectified linear unit (ReLU)-type functions) have been used in many

137   studies (Pal et al., 2019; Liu et al., 2020; Roh and Song, 2020; Ukkonen et al., 2020;

138   Veerman et al., 2020), the best activation function that is used for the radiation emulator is

139   still controversial. The development of DNN emulators has included several sensitivity

140   experiments investigating the number of neurons and hidden layers (Pal et al., 2019; Liu et al.,

141   2020; Veerman et al., 2020; Meyer et al. 2021); however, no attempt has yet been made to

142   investigate the radiation process at the same computational cost (or speedup the process). Pal

143   et al. (2019) compared the validation loss architecture of 32-32-32 (32 neurons and 3 hidden

144   layers) with 16-16-16 (16 neurons and 3 hidden layers), 32-32-32-32 (32 neurons and 4

145   hidden layers), and 64-64-64 (64 neurons and 3 hidden layers), but the computation costs of

146   the experiments differed because the numerical complexity is expressed as the total

147   dimension of the weight and bias coefficients. Furthermore, the use of a single hidden layer,

148   which can include the largest number of neurons at the same computational cost, was not

149   considered in Pal et al (2019). Belochitski and Krasnopolsky (2021) emphasized the risks of

150   using the DNN emulator in relation to increasing nonlinearity, and retained the use of a single

151   hidden layer in developing the NN emulator for radiation parameterization. However, no

152   practical evidence was provided (i.e., the DNN experiments were not performed), indicating

153   that the accuracy of NN (with a single hidden layer) and DNN (with multiple hidden layers)

154   emulators still requires comprehensive evaluation at the same computational cost and

155   numerical complexity. Sensitivity tests with different batch sizes have rarely been performed

156   in the field of radiation emulation, except for the speedup check that was reported in Liu et al.

157   (2020). In general, the use of an appropriate mini-batch is known to produce a more accurate

158   solution than the full batch (Li et al., 2014), while requiring more training (a small batch size

159   is equivalent to less parallelization). Thus, further consideration of batch size may contribute

160   to optimizing the performance of the radiation emulator.

161   Stochastic weight averaging (SWA), which was recently developed in the field of

162   machine learning, is aimed at increasing generalization in the NN training process (Izmailov

163   et al., 2018). In general, a multi-model ensemble approach is used to reduce the uncertainty in

164   a single model. However, this approach is not appropriate for use in emulators that are used

165   to speed up the GCM and NWP because the computational burden is directly proportional to

166   the number of ensemble members included. As an alternative approach in which the

167   computational cost can be minimized, SWA performs the averages for multiple points along

168   the trajectory of the stochastic gradient descent (SGD) (Bottou, 2012; Mandt et al., 2017)

169   under constant or cyclical learning rates. SWA tends to find a wide flat solution using this

170   method, whereas the SGD often converges to a sharp (or local) minimum that can cause

171   problems with generalization. Izmailov et al. (2018) noted that the use of SWA can improve

172   the accuracy of test sets with better generalization than conventional SGD in terms of several

173　benchmarks. To the best of our knowledge, SWA has never been used in climate and weather

174　models. In fact, as noted by Krasnopolsky et al. (2008), Belochitski and Krasnopolsky (2021),

175　and Song et al. (2021), emulator studies using the GCM and NWP face severe problems with

176　generalization because the errors that are accumulated during long-term integration by the

177　emulator can induce a blow-up of the entire numerical model. Because infinite training

178　datasets cannot be used, generalization is an important issue for developing universal

179　radiation emulator.

180　　This study therefore mainly examines the benefits of using SWA in developing a

181　radiation emulator for the NWP model under the frameworks of idealized squalline and real

182　case simulations. The ideal simulation will then serve as a testbed for various sensitivity

183　experiments. At the same computational cost, the results of SWA will be compared with NN

184　based on sequential training (SNN), which has been used in many previous studies

185　(Krasnopolsky et al., 2005, 2008, 2010; Belochitski et al., 2011; Roh and Song, 2020;

186　Belochitski and Krasnopolsky, 2021; Song and Roh, 2021; Song et al., 2021), and the

187　infrequent use of radiation scheme, which is a popular method in operational NWP fields

188　(Pauluis and Emanuel, 2004; Pincus et al., 2013). Sensitivity experiments investigating the

189　sampling ratio of training sets, activation functions, the number of hidden layers (at the same

190　speedup), and batch sizes (as well as learning rates) are also conducted. These all efforts will

191　contribute to reducing the forecast error of the NWP model using the NN radiation scheme

192　that can attain significant speedup.

193　**2. Data and Methods**

194　　This study considers two types of frameworks (i.e., ideal and real cases) to evaluate the

195　performance of a radiation emulator based on the Advanced Research Weather Research and

196　Forecasting (WRF-ARW) model (Skamarock et al., 2019). The ideal framework was based

197　on a two-dimensional squall-line simulation with 5-km resolution on 201 horizontal grids,

198 using 39 vertical layers up to 50 hPa and a 24-h integration period with a model time step (dt)

199 and radiation time step (radt) of 20 s serving as the control run for the ideal simulation.

200 Different horizontal resolution (0.25 km → 5 km), integration time (6 h → 24 h), and time

201 steps (3 s → 20 s) than those used in Roh and Song (2020) allowed consistency with the real

202 case experiment. Thus, this experiment can provide conceptual guidance for large-scale

203 datasets generated under real conditions. The use of small-scale data rendered it possible to

204 perform various sensitivity experiments. For the real case, this study used the horizontal

205 domain with 234×282 grids over the Korean peninsula, which is the same that utilized in the

206 Korea Local Analysis and Prediction System (KLAPS), one of the operational NWP models

207 used by the KMA. Note that the dynamics and physics processes of the KLAPS were based

208 on the WRF model. The radiation emulator used in both ideal and real case frameworks

209 targets the RRTMG-K radiation scheme (Baek, 2017), which calculates vertical heating rates

210 and LW fluxes with 256-g points in 16 bands and SW fluxes with 224-g points in 14 bands.

211 The WRF double moment 7-Class (WDM7) microphysics scheme (Bae et al., 2019) was used

212 in both simulations. The real case simulation further used the KIAPS Simplified Arakawa–

213 Schubert (SAS) cumulus (Kwon and Hong, 2017), the Shin and Hong planetary boundary

214 layer (Shin and Hong, 2015), the revised MM5 Monin–Obukhov surface layer (Jiménez et al.,

215 2012), and the Unified Noah land surface model (Tewari et al., 2004). The RRTMG-K

216 scheme accounted for 85.0% (for the ideal case) and 88.6% (for the real case) of the total

217 computational costs of using the WRF model under the same dt and radt (20 s). The ideal and

218 real case frameworks were initialized by default initial sounding in the WRF model (with

219 warm bubble forcing at low levels) and data from the European Center for Medium-Range

220 Weather Forecasts Reanalysis v5 (ERA5) (Hersbach et al., 2020) with 0.25° grid and 3-h

221 intervals, respectively.

222   The training sets for the ideal simulation were prepared through random sampling of the

223   full set (i.e., control run for 24 h) using sampling ratios from 10% to 90%. The representation

224   error was reduced under an increase in the sampling ratio. However, the ideal experiment is a

225   highly nonlinear system that is sensitive to small perturbations in the initial stage; therefore,

226   the radiation emulator was found to produce quite different results during the 24-h integration

227   over 201 grids (i.e., the emulator was applied 868,320 times) when it was applied to the WRF

228   model (i.e., via online prognostic testing). Thus, we did not expect a consistent trend with the

229   sampling ratio. The training sets were divided into LW clear, LW cloud, SW clear, and SW

230   cloud to maintain consistency with the input–output structure of the radiation emulator

231   developed by Song and Roh (2021). The training sets for the real case simulations were sub-

232   sampled from 10-min interval outputs from the period 2009–2019, with 48 days from the

233   period of 2009–2018 and the one-year period of 2019 used in Song and Roh (2021) evenly

234   considered (i.e., 50% of the 48 days and 50% in 2019). Note that the 48 days included events

235   on which the maximum and the second maximum precipitation occurred in each month

236   together with non-precipitating 24 days over the period of 2009–2018. To optimize the

237   hyperparameters used in the NN training, we further prepared independent validation sets

238   consisting of the days on which the third and fourth maximum precipitation occurred in each

239   month over the period of 2009–2018 along with other non-precipitating 24 days which were

240   not used in the training sets. Note that the validation sets were newly adopted in this study

241   because Song and Roh (2021) did not optimize the hyperparameters. The training and

242   validation sets were divided into 96 categories with 3 million cases in each, as in Song and

243   Roh (2021), who used a 96-categories approach (LW and SW, clear and cloud, land and

244   ocean, and 12 months) to effectively utilize as much data as possible to reduce the

245   representation error. The final evaluation of accuracy was performed for the year 2020 using

246   a one-week period and 3-h intervals (test sets), while the emulator was implemented in the

247   WRF model (i.e., online prognostic testing). Note that the one-week forecast period used in

248   this study was much extended compared to the one-day period used in Song and Roh (2021).

249   The inputs for the NN emulator for the ideal simulation consist of 187 variables,

250   including: pressure (39 profiles), temperature (39 profiles), water vapor (39 profiles), ozone

251   (39 profiles), and cloud fraction (30 profiles due to the removal of constant values), in

252   addition to skin temperature (LW) and the solar constant multiplied by the cosine zenith

253   angle (SW). The inputs were decreased by 157 variables in the clear case, because the cloud

254   fraction was not used. The inputs for the real case simulation further included surface

255   emissivity (LW), surface albedo (SW), and monthly variant cloud fraction (28 to 35 profiles).

256   Unlike Song and Roh (2021), topography (longitude, latitude, and elevation) was excluded in

257   this study. The outputs for both the ideal and real case simulations consist of 39 heating rate

258   profiles and three fluxes (upward fluxes at the top and bottom, and downward flux at the

259   bottom). Hereafter, the heating rate and flux in this study refer to the heating rates in the 39

260   layers and the three fluxes, respectively. The inputs and outputs are summarized in Table 1.

261   For given input–output pairs, two NN methods were applied: SNN (Krasnopolsky, 2014) and

262   SWA (Izmailov et al., 2018). Both are fully connected and feed-forward NN methods. Here,

263   the same min-max normalization and standardization were used for the inputs and outputs,

264   respectively. In addition, because the SNN provides the utility of early stopping, the

265   maximum number of epochs used in SWA was determined from the SNN. The SWA mode

266   was applied to the last 25% of the epochs, as in Izmailov et al. (2018), while the former 75%

267   of the epochs was trained by the common SGD. Under the ideal simulation, the mean and

268   standard deviation of epochs were 13,499±4697 for clear and 4,089±832 for cloud cases

269   with different sampling ratios of 10–90%. When the number of samples is large, the required

270   epoch tends to decrease. For the real case, the mean of 3,011 epochs was used for clear and

271 2,251 for cloud conditions; thus, approximately 3,000 and 2,200 epochs were used,

272 respectively.

273   After the NN training, the weight and bias coefficients were obtained and inserted into the

274 radiation emulator, replacing the RRTMG-K code (module_ra_rrtmg_swk.F) in the WRF

275 model. In the emulator code, the NN outputs were forced into the range between the

276 minimum and maximum values of the training sets to prevent extrapolation. Because the

277 numerical complexity in the NN is defined as the total sum of the dimensions of the weight

278 and bias coefficients, the use of 90 neurons in a single hidden layer for the radiation process

279 corresponds to a 60-fold speedup and an 87% reduction in the total computation time (Song

280 and Roh, 2021). We follow this methodology for the real case simulation. For the ideal case,

281 the mean computation time for the radiation process and the total model were measured using

282 the Intel Xeon E5-2690v3 central processing unit (CPU) with serial compilation condition.

283 As a result of averaging 10 experiments, a mean speedup of 60 times (3086 s ÷ 51.5 s) was

284 achieved for the radiation processes and the time taken to run the total model was 84% (3630

285 s vs. 593.5 s) lower. The small difference observed between the results obtained using the

286 SNN and SWA was thought to be due to different cloud conditions during integration. For the

287 situation in which there are the same number of neurons in the hidden layers, the numerical

288 complexity of the NN or DNN can be expressed as: $I \times N + N + (H–1) \times (N \times N + N) + N \times O + O$.

289 Here, I is the number of input variables, O is the number of output variables, N is the

290 number of neurons, and H is the number of hidden layers. For example, 68-68 (two hidden

291 layers), 58-58-58 (three hidden layers), 52-52-52-52 (four hidden layers), and 47-47-47-47-

292 47 (five hidden layers) neuron structures are comparable to 90 neurons with a single hidden

293 layer in terms of producing a 60-fold speedup. This is a fair approach in terms of

294 computational cost, unlike the sensitivity experiments in Pal et al. (2019), Liu et al. (2020),

295 Ukkonen et al. (2020), and Veerman et al. (2021). These comparisons can be used to obtain

296   an answer to the controversial argument raised by Belochitski and Krasnopolsky (2021), who

297   discussed the use of a single hidden layer (with a long history) and multiple hidden layers in

298   developing an NN emulator for radiation parameterization.

299   In conclusion, the idealized squalline simulation was used to perform the sensitivity

300   experiments using sampling ratios from 10–90% in generating a training set. Both SNN and

301   SWA methods were applied, and their accuracy was measured in terms of the root mean

302   square error (RMSE) by comparing with the control run over 24 h. As in a previous study

303   (Song and Roh, 2021), the 60-fold speedup (i.e., 90 neurons) emulator results were also

304   compared with the infrequent radiation scheme with a radt of 20 m (denoted as "WRF60" in

305   this study). Here, we did not adjust the time between the infrequent calls, as in Manners et al.

306   (2009) and Hogan and Bozzo (2015), because the treatment was not available in the

307   WRF model. To minimize the redundancy problem, a sampling ratio of 10% was selected

308   and then applied to subsequent experiments. For the second experiment, sensitivity tests were

309   conducted with 16 nonlinear activation functions (Tanh, Arctan, Tanhshrink, Sigmoid,

310   Logsigmoid, SiLU, Softsign, Softplus, Mish, Hardtanh, Hardsigmoid, Hardswish, ReLU,

311   LeakyReLU, ELU, and SELU) based on SWA. Detailed definitions of the activation

312   functions are presented in Table 2. The SWA results were evaluated with SNN using Tanh.

313   The third experiment involved sensitivity tests on the number of hidden layers (1–5). The

314   numerical complexity, and thereby speedup, for the radiation process was maintained by

315   reducing the number of neurons in a given hidden layer. Different speedup conditions of 15,

316   30, 45, 60, 90, and 120 times were considered in the ideal simulation. The best performance

317   for each speedup condition was selected from the mean RMSEs using five prediction

318   variables (LW/SW heating rates, LW/SW fluxes, and surface temperature) over 24 h. In real

319   case simulation, experiments for batch sizes and learning rates were performed for validation

320   sets. The experiment based on huge datasets (96×3 million data) was found to be extremely

321   time consuming compared to the ideal case. In fact, the SNN based on sequential training

322   with one batch size (Krasnopolsky, 2014) is fundamentally different from the batch learning

323   in SWA (or SGD). In addition, SNN was performed using adjustable learning rates (10^{-3} to

324   10^{-6}) during the NN training and generally converged at optimal solutions of approximately

325   2,000 and 1,200 epochs with a learning rate of 10^{-4}. Smith et al. (2018) insisted that batch

326   size and learning rate should be proportional to achieve similarly high performance among

327   the experiments. The empirical relationship observed between batch size and learning rate

328   under the SNN (1 and 10^{-4}) was thus applied to the experiments investigating batch sizes

329   (100–9000) and initial learning rates (0.001–0.9) in the SWA. It should be noted that the

330   learning rate of the SWA mode was reduced by half of its initial value under cosine annealing.

331   The computation time taken for training all datasets (i.e., 96 sets) was 12 h using the NVIDIA

332   DGX A100 graphics processing unit (GPU) 16 units, in contrast to the 63 h taken by the SNN

333   using 96-node parallelization that was carried out with the Intel Xeon E5-2690v3 CPU. The

334   computation time taken by the GPU for training was based on a batch size of 500 (which will

335   be further discussed later). The learning rate of the SWA in the ideal simulation was

336   determined empirically by multiplying the full batch size (equal to the number of datasets) by

337   2×10^{-6} based on a learning rate of 0.92997, which is less than 1 for the maximum number of

338   datasets (464,985). Note that there were 316,322 LW clear, 464,985 LW cloud, 115,103 SW

339   clear, and 215,821 SW cloud datasets for the sampling ratio of 90%, and the numbers were

340   reduced proportionally to the sampling ratio. No further experiments were performed on

341   batch size or learning rate in the ideal simulation, although the use of mini-batches and a

342   proper learning rate may lead to better optimization. The SWA group with the highest

343   accuracy in the validation sets (2009–2018) was used in the final online testing for the year

344   2020. The RMSE evolutions during a one-week period were examined for LW/SW fluxes,

345   skin temperature, 2-m air temperature, and 3-h accumulated precipitation. The evaluation of

346   2-m temperature and precipitation was performed by comparing with surface observation in

347   South Korea, and the other variables were compared with the control run and WRF60. The

348   real case experiments on multiple hidden layers (2–5) were further examined in the final

349   evaluation step.

350   **3. Results and Discussion**

351   For the idealized squall line simulation, nine-type datasets with a sampling ratio ranging

352   from 10% to 90% were trained by the SNN and SWA methods. The two methods were based

353   on Tanh. The mean RMSEs for five variables are compared with the results of the control run,

354   which was executed over 24 h in 1-min intervals over the 1000-km domain in Fig. 1 (LW/SW

355   heating rates, LW/SW fluxes, and surface temperature). The emulator results were used 4,320

356   times temporally (number of time steps) and 201 times spatially (number of grids). Only

357   daytime variables were considered in the RMSE calculation of SW radiation. No apparent

358   dependency on the sampling ratio was observed in either SNN or SWA. Although the

359   representation error should decrease when the sampling ratio is increased, the strong

360   nonlinearity of the ideal simulation appears to have significantly influenced the results over

361   24 h. We can also suspect a strong correlation between training sets because 5-km and 20-s

362   interval data were used. In such a situation, finding an optimal sampling ratio for NN training

363   using advanced sampling techniques can be helpful and should be investigated in the future.

364   Compared to the SNN, improvements of 9.9% were observed in the mean RMSE for all

365   sampling ratios by using SWA, indicating that SWA can guarantee a better performance than

366   SNN, regardless of the datasets used. Because the NN approximation tends to be optimized to

367   reduce the total error, the improvements are not linear for all variables. On average, the SW

368   heating rate showed the largest improvement (20.7%) of the five variables, and can increase

369   the predictability during the daytime. Roh and Song (2020) also noted that the SW heating

370   rate is the most uncertain variable among radiation products. The uncertainty of the SW

371   heating rate is thought to be significantly reduced by using SWA. For a sampling ratio of

372   10%, the mean RMSE improvements generated by using SWA for the five variables were

373   13.2% higher than errors involved in using SNN (23.20% vs. 10.03%). The improvements in

374   the RMSE obtained by using SWA were relatively large for the SW outputs (12.2–20.7%).

375   The difference between SNN and SWA was large for small sampling ratios (10% and 30%,

376   respectively), which is thought to be because SWA can better generalize the training results

377   compared to common NN (Izmailov et al., 2018). Because all of the data covering natural

378   variability can be obtained, this benefit of using SWA is expected to exert a strong influence

379   and improve the performance in the real-case simulation.

380   These results suggest that datasets based on a 10% sampling ratio with the smallest

381   redundancy should be used. The activation function is an important hyperparameter that can

382   significantly affect the performance of emulator because it is used not only in the learning

383   process but also in the emulator code (within the WRF model). The SWA results using 16

384   activation functions (Tanh, Arctan, Tanhshrink, Sigmoid, Logsigmoid, SiLU, Softsign,

385   Softplus, Mish, Hardtanh, Hardsigmoid, Hardswish, ReLU, LeakyReLU, ELU, and SELU)

386   are compared with the results obtained by SNN based on Tanh in Fig. 2, together with the

387   RMSEs for 24 h over the 1000-km domain. The mean and standard deviation of RMSEs

388   varied by 2.21 ± 0.12 K day^{-1} for LW heating rate, 0.98 ± 0.06 K day^{-1} for SW heating rate,

389   12.19 ± 1.63 W m^{-2} for LW flux, 118.93 ± 19.58 W m^{-2} for SW flux, and 0.86 ± 0.10 K for

390   surface temperature. Some activation functions (e.g., Arctan and Hardswish) showed worse

391   performance than SNN. The lowest error among the SWA experiments was observed when

392   Tanh was used. This feature is in line with many emulator studies based on Tanh

393   (Krasnopolsky et al., 2005, 2008, 2010; Belochitski et al., 2011; Roh and Song, 2020;

394   Belochitski and Krasnopolsky, 2021; Chantry et al., 2021; Song and Roh, 2021; Song et al.,

395   2021), and we therefore used Tanh for subsequent experiments.

396   Figure 3 shows the temporal and horizontal evolution for the LW/SW upward fluxes at

397   the top (LWUPT/SWUPT), surface temperature, and precipitation rate at 1-min intervals. The

398   control run, SNN, and SWA results (radt = 20 s) were compared with those of WRF60 (radt =

399   20 m). The SNN, SWA, and WRF60 have the same computational cost with an 84%

400   reduction compared to the control run. The control run shows evolutionary features in two

401   directions (i.e., positive and negative X directions) that are initialized at the center position (0

402   km). The highest SWUPT (an indicator of deep clouds) and the lowest surface temperature

403   areas were observed along the positive X direction. These areas are associated with a

404   squalline precipitating system. This squalline feature was not evident in Roh and Song (2020),

405   probably because of a strong interaction between radiation and microphysics in the small

406   domain (50 km), although this experiment showed the squalline feature in the microphysics

407   scheme only. In the negative X direction, low LWUPT and high SWUPT (an indicator of

408   clouds) and low surface temperature areas are characterized by non-precipitating clouds (e.g.,

409   anvils). The forecast error is more evident in the cloud areas. Interestingly, WRF60 showed

410   discontinuous features for LWUPT and SWUPT, which are direct outputs from the radiation

411   scheme, because the radiation scheme was used 60 times (radt = 20 m) less than the dt of 20 s.

412   This problem was not found in the results of SNN and SWA because radt of 20 s was used, as

413   in the control run. Overall, evolutionary features of the squalline system appear to have been

414   properly simulated in both SNN and SWA.

415   The time series of the RMSEs for the five variables are shown in Fig. 4. The simulation

416   was initialized at midnight and then integrated for 24 h. The zero SW heating rate and flux

417   (i.e., nighttime) were excluded from the analysis. In WRF60, the RMSEs for the LW heating

418   rate and flux tended to increase substantially with integration time because the error due to

419   the use of the infrequent radiation scheme accumulated during integration. The RMSEs of

420   SW heating rate and flux were largest around noon in association with the strong incident SW

421 radiation. The RMSEs of LW heating and flux decreased substantially after sunset when the

422 effects of the SW radiation disappeared. The SNN results show an improved RMSE pattern

423 as a whole compared to WRF60, with improvements evident for all variables before noon.

424 However, the RMSE improvements tended to weaken in the afternoon. This clearly reveals

425 the fundamental problem of radiation emulator, which is associated with accumulated errors

426 during integration (Krasnopolsky et al., 2008; Song et al., 2021). Using SWA alleviated the

427 problem that appeared when using SNN. Before 4 h, SWA showed a larger error than SNN

428 for the LW heating rate, flux, and surface temperature. However, after 4 h, SWA produced

429 significantly lower RMSEs for all variables. The RMSE improvements associated with SWA

430 were evident in relation to the SW radiation during daytime. The largest improvement among

431 the five variables was observed in the SW heating rate, as seen in Fig. 1. Around sunset and

432 afterwards, the RMSE improvements gained by using SWA tended to decrease, indicating

433 that the results are affected by the daily solar cycle; this assumption can be confirmed using

434 the results obtained over multiple days in the subsequent real case simulations (i.e., one

435 week). The total statistics of the ideal simulations are summarized in Table 3. In terms of the

436 total improvement for the five variables compared with WRF60, the performance of the SNN

437 with 60-fold speedup was located between WRF9 with 9-fold speedup (radt = 3 m) and

438 WRF30 with 30-fold speedup (radt = 10 m). In contrast, the SWA results were even better

439 than those of WRF9. Note that WRF9 performed the best among the infrequent uses of

440 radiation scheme with radts of 1 m to 5 m. These results suggest that SWA can produce more

441 accurate and fast results compared with the operational method based on infrequent radiation

442 scheme.

443   Before examining the real case simulation, we further examined the effect of multiple

444 hidden layers (i.e., DNN) on the SWA emulator under the idealized squalline framework.

445 Here, we focus on six speedup conditions of 15, 30, 45, 60, 90, and 120 times for the

446 radiation process, which correspond to 360, 180, 120, 90, 60, and 45 neurons in a single

447 hidden layer. For each speedup condition, we considered DNN structures with two to five

448 hidden layers that have the same numerical complexity as a single hidden layer. For example,

449 in relation to 60-fold speedup, 90, 68-68, 58-58-58, 52-52-52-52, and 47-47-47-47-47

450 neurons were used for one, two, three, four, and five hidden layers, respectively. Figure 5

451 shows that the use of a single hidden layer produced the lowest error among all experiments

452 under the same speedup conditions. Note that dark gray colors predominated in the single

453 hidden layer (Fig. 5) and the use of multiple hidden layers showed 7.41–9.80% degradation

454 compared to the single hidden layer on an average of six speedup cases in terms of the mean

455 RMSE improvement for five variables compared with WRF60. This is thought to be related

456 to the reduction in the number of neurons used for the DNN and provides experimental

457 evidence for the conceptual argument by Belochitski and Krasnopolsky (2021) that the

458 nonlinearity of the DNN can be rapidly increased owing to the complex structure of hidden

459 layers, which can lead to more unstable generalization such as nonlinear extrapolation.

460 Vapnik (2019) also noted that the use of DNN does not always guarantee the best solution for

461 a given problem. However, this result was based on one ideal case from which we cannot

462 draw general conclusion regarding the usefulness of the DNN in developing radiation

463 emulator.

464   As described in the Data and Methods section, the real case simulation was primarily

465 based on KLAPS, which is one of the operational NWP models in the KMA. The training

466 sets were based on the period between 2009 and 2019. The 48 days that were not used for

467 training data were used as the validation sets to optimize the hyperparameters in the SWA.

468 This can be considered as offline testing, whereas the final evaluation for the year 2020

469 connected with WRF modeling was tested online. Unlike the online prognostic test, which is

470 affected by the integration of the numerical model, the accuracy of the offline test should be

471   relatively high because the error does not accumulate. In the offline test, we mainly examined

472   the optimization of the batch size and learning rate in the SWA method. The batch size is an

473   important hyperparameter in determining the fundamental difference between SNN, which is

474   based on sequential training (batch size = 1), and SWA, which is based on batch training

475   (batch size > 1). Reducing the batch size (i.e., the use of mini-batches) and learning rate can

476   lead to better performance in general; however, Smith et al. (2018) insisted that batch size

477   and learning should be proportional to each other. Here, we empirically forced a proportional

478   relationship of 10^{-4} between batch size and learning rate based on the relationship observed in

479   the SNN (1 and 10^{-4}). Because the use of too small batch size (i.e., less parallelization) led to

480   a substantial increase in the training speed, we empirically set the minimum batch size as 100.

481   The batch size was extended to 1000 with 100 intervals and 9000 with 1000 intervals. The

482   corresponding learning rates were 0.001 to 0.9. Figure 6 shows the validation results for the

483   LW/SW heating rates and LW/SW fluxes. Here, 12 months, land/ocean, and clear/cloud

484   results were averaged. The fraction of land over the entire domain was 45.3% and the mean

485   fraction of cloud was assumed to 50%. Regardless of the batch sizes and learning rates used,

486   SWA exhibited superior performance compared to SNN. On average of 10 experiments, the

487   RMSEs of the LW/SW heating rates and LW/SW fluxes were improved by 3.15%, 8.68%,

488   7.92%, and 9.70%, respectively, compared with the RMSEs obtained using SNN (0.4740 K

489   day^{-1}, 0.1968 K day^{-1}, 3.9140 W m^{-2}, and 21.6417 W m^{-2}, respectively). Among the 10

490   experiments, the result obtained with a batch size of 500 and a learning rate of 0.05 showed

491   the best performance with RMSE improvements by 3.21%, 10.21%, 8.18%, and 11.59% for

492   the LW/SW heating rates and LW/SW fluxes, respectively. Similar to the ideal simulation,

493   there were relatively large improvements in the SW outputs. These results reveal the

494   characteristics by which SWA strengthens generalization at the expense of training accuracy

495   (Izmailov et al, 2018). The obtained settings (500 and 0.05) were thus used to evaluate the

496   final performance of the online testing results in the real-case simulation.

497   Figure 7 represents the spatial distribution of LWUPT, SWUPT, and skin temperature for

498   a real-case example (typhoon HAISEN, 12LST September 17, 2020). The typhoon is the

499   most extreme weather phenomena that occur over the Korean peninsula. Since it was

500   initialized on 00LST September 1, this case corresponds to a 6.5-day forecast result; thus, the

501   radiation scheme used 28,080 time-steps (with a radt of 20 s). Note that this is a more long-

502   term result compared with the 12-h forecast result for typhoon SANBA in Song and Roh

503   (2021). Despite the 156-h forecast, the SNN and SWA emulator results show similar patterns

504   to the WRF control run, with differences in the detailed patterns. The LWUPT and SWUPT

505   around the typhoon were characterized by low and high values, respectively; mainly over the

506   northern part of the Korean Peninsula. These areas were also connected to cold surface

507   temperatures. During the event, the RMSEs for LWUPT and SWUPT in the SNN (SWA)

508   were improved by 11.11% (10.89%) and 6.08% (6.84%), respectively, compared to WRF60

509   (13.68 W m^{-2} and 138.92 W m^{-2}). However, SNN exhibited a 15% higher RMSE for skin

510   temperature. This feature was significantly improved by using SWA, with a 1% decrease in

511   RMSE compared to WRF60, implying that SWA produces more stable results.

512   More generalized evaluations of the total cases are shown in Fig. 8, in which 48 real-case

513   simulations are presented. Each simulation was initialized on the 1st, 8th, 15th, and 22nd of

514   each month in 2020 and then integrated for one week. Thus, 29–31 days in each month were

515   excluded from the analysis. Each RMSE at a given 5-km grid in Fig. 8 represents a statistical

516   result for a one-week forecast over 48 cases in 2020. As shown in Fig. 7, both SNN and SWA

517   tended to improve the forecast accuracy of LW/SW fluxes compared with WRF60, and SWA

518   showed further reduced RMSEs for LW flux, SW flux, and skin temperature than SNN.

519   Relatively large errors of LW flux and skin temperature remain in the mountainous area of

520   North Korea. A more quantitative analysis is presented in Fig. 9. The RMSE time series

521   denotes a statistical result over 226×274 grids (excluding ±4 boundary points) and 48 weeks

522   at 3-h intervals (totaling 166 million data points). In Fig. 9a, the RMSE for the LW flux under

523   WRF60 tended to increase rapidly before 2 day, and then steadily fluctuated with diurnal

524   perturbation observed after 2 day. The improvements in the RMSE of the LW flux for SNN

525   (compared to the WRF60) decreased substantially from 15.5% before 1 day to only 1.4%

526   after 6 days (Fig. 9a). This represents a weakness in the radiation emulator that the

527   accumulation of errors caused by the NN approximation can be rapidly amplified in long-

528   term forecasts. However, because the SWA method is effective in reducing the uncertainty,

529   the RMSE improvements seen in the LW flux were 19.7% before 1 day and 9.0% after 6 day

530   (Fig. 9a). In particular, the RMSE of the LW flux after 6 day was 7.8% lower using SWA

531   than that obtained using SNN. For the SW flux (Fig. 9b), the time series of the RMSEs were

532   relatively similar to those for the LW flux. Looking at the maximum RMSEs of SW flux

533   around noon, the SNN and SWA emulators showed smaller RMSEs until 5 day, whereas the

534   SNN results produced the largest error after 5 day. Thus, we can assume that the rapid

535   increase in the RMSE of the LW flux is also affected by SW radiation. Note that the mean

536   RMSE of SW flux for the SNN decreased by 8.8% after 5 day, whereas that of the SWA

537   improved by 6.3% compared to WRF60. For skin temperature, both emulator results showed

538   degradation after 4 day (Fig. 9c). The maximum RMSEs of skin temperature during both

539   daytime and nighttime were larger than those of WRF60, whereas SWA was better than SNN.

540   Skin temperature is not a direct output of the radiation scheme, and it can interact with other

541   processes in a complex manner. In determining skin temperature, it is thought that the

542   influence of clouds (e.g., the amount and location of clouds) will be greater than that of the

543   radiation process. This can lead to an interpretation of Fig. 9d, which shows the evaluation

544   results with 2-m temperature observations in South Korea. In Fig. 9d, while the RMSEs were

545 distributed over 1.9–2.7 K, the difference obtained from the various experiments was

546 relatively small. The final RMSEs are listed in Table 4. The RMSEs were 2.2438 K for

547 WRF60, 2.2466 K for SNN, and 2.2563 K for SWA, and their difference was much smaller

548 than the observation error (0.1 K). Similar results were also found in the evaluation of

549 precipitation compared with the gauge-radar merged observations in South Korea (Fig. 10),

550 with RMSEs of 12.1987–12.3120 mm (Table 4). The standard deviation of the RMSEs was

551 only 0.4% of the mean RMSE obtained for precipitation. As noted by Song and Roh (2021),

552 because the control run also had errors as compared with observation, the error induced by

553 the use of a radiation emulator can be insignificant in terms of observation. Instead, the

554 uncertainty associated with clouds can play a more important role in determining surface

555 temperature. Even so, these results imply that the radiation emulators in this study produce

556 accurate one-week forecasts at the NWP level, in addition to a significant 60-fold speedup. In

557 this context, the use of SWA guarantees robust results in terms of speed, accuracy, and

558 stability. The RMSEs for both emulators were between those of WRF30 and WRF60 (Table

559 4).

560　　　When multiple hidden layers and a small number of neurons (i.e., keeping the same 60-

561 fold speedup) were considered, the RMSEs for the one-week forecast changed (Table 4).

562 Here, 90, 68, 58, 52, and 48 neurons were used in 1–5 hidden layers (1 h to 5 h), respectively.

563 Among the five SWA experiments using the different numbers of hidden layers, the use of

564 two hidden layers showed the lowest RMSEs for LW/SW fluxes and skin temperature,

565 exhibiting 0.4–1.3% lower RMSEs compared with the use of one hidden layer. As a result,

566 the RMSEs of LW/SW fluxes and skin temperature were improved by 12.6%, 8.0%, and 4.4%

567 compared with those of WRF60. The use of four and five hidden layers resulted in a worse

568 performance than the results obtained with one hidden layer. This implies that there is an

569 optimal number of hidden layers for a given problem. Gentine et al. (2018) and Pal et al.

570 (2019) also used three and eight hidden layers as the optimal numbers of hidden layers,

571 respectively, when developing their emulators. In a similar context, the use of an optimizer

572 for tuning hyperparameters (e.g., Hertel et al., 2020), including the number of neurons and

573 hidden layers, may improve the accuracy of the training data, but it does not always

574 guarantee the generalized performance using independent test data (e.g., the overfitting

575 problem). However, the RMSEs for 2-m temperature and precipitation among the

576 experiments using different hidden layers changed within 1%, implying that the operational

577 use of the developed emulator is possible as it is now.

578 **4. Summary and Conclusions**

579   This study examined the performance of a radiation emulator based on SNN and SWA

580 training methods under idealized squalline and real case (over the Korean peninsula)

581 frameworks. Both frameworks used the WRF model with 5-km horizontal resolution, 39

582 vertical layers, a model/radiation time step of 20 s, and the RRTMG-K radiation scheme.

583 Ideal and real case simulations were integrated for 24 h and 168 h, respectively. Input

584 variables of 157–187 (ideal) and 158–190 (real), and 42 output variables were prepared, and

585 90 neurons with a single hidden layer were used in the NN training. The variables were

586 further separated into four categories (LW/SW and clear/cloud) in the ideal simulation and 96

587 categories (LW/SW, clear/cloud, land/ocean, and 12 months) in the real case simulation. The

588 weight and bias coefficients obtained from the NN training were implemented in the WRF

589 model by replacing the RRTMG-K code. The resultant radiation process was speed up 60

590 times with a total reduction in the computation time of 84–87%. In the ideal simulation,

591 sensitivity experiments were conducted examining the sampling ratio, activation functions,

592 and number of hidden layers. Regardless of the sampling ratios, SWA improved the RMSEs

593 by 10% as compared to SNN. At a sampling ratio of 10%, the performance increased even

594 further to 13.2%. Compared to the infrequent use of radiation scheme by 60 times, SNN

595   improved RMSEs by 5.8–14.1% for five forecast variables, and SWA further increased these

596   improvements by 18.2–26.9%. Among the 16 activation functions, the use of Tanh showed

597   the best performance. However, even if multiple hidden layers were considered, the

598   performance was not superior to that of the single hidden layer in the ideal simulation. The

599   final performance of the SWA was better than operational methods based on infrequent

600   radiation scheme by 3 to 60 times, suggesting improvements in both accuracy and speed for

601   SWA emulator. The ideal framework served as the testbed for various sensitivity experiments

602   before the real case simulation, which requires significant computational effort.

603   In the real case simulation, the training sets were prepared for the period 2009 to 2019. To

604   optimize batch size and learning rate, independent validation sets were prepared. After 10

605   sensitivity experiments based on the SWA, the optimal batch size and learning rate were

606   determined to be 500 and 0.05, respectively. This contributed to the mean RMSE

607   improvement averaging 8.30% for the four variables (LW/SW heating rates and fluxes)

608   compared to the SNN that was based on sequential training with one batch size. In a case

609   study, both emulators properly simulated the 156-h forecast patterns of typhoon HAISEN

610   (12LST September 17, 2020). However, SWA showed better performance for predicting skin

611   temperature with a 14% reduction in the RMSE compared to SNN. The final evaluation was

612   performed for 2020. Here, 48 cases were initialized from 1, 8, 15, and 22 days of each month,

613   which were then integrated over one week. Compared to WRF60, SNN showed 8.8% and 4.7%

614   RMSE improvements for LW and SW fluxes; however, these improvements deceased

615   significantly after a 5-day forecast, resulting the RMSE of skin temperature was increased by

616   1.8%. By contrast, the use of the SWA solved this problem, and the resultant RMSE

617   improvements were 12.3%, 7.2%, and 3.2% for LW flux, SW flux, and skin temperature,

618   respectively, compared to WRF60. These RMSEs were further improved by the use of two

619   hidden layers, to 12.6%, 8.0%, and 4.4%. This is in contrast to the ideal experiment, which

620 showed the best performance under the use of a single hidden layer. Therefore, we can

621 conclude that the use of multiple hidden layers can be helpful for optimizing forecast

622 accuracy, but it does not always guarantee better performance owing to the constraint of

623 computational cost (i.e., a smaller number of neurons should be used in the DNN). When

624 compared with surface temperature and precipitation observations, the maximum RMSE

625 difference between experiments (control run, infrequent methods of radiation scheme, and

626 emulators) was less than 1%, confirming the robustness of the developed emulators.

627 The radiation emulators in this study will replace the radiation scheme of the KMA

628 operational short-range weather forecasting model over the Korean peninsula. The one-year

629 evaluation suggests that the use of this scheme can contribute to maintaining accuracy while

630 significantly improving the computational speed of the NWP model. Operational

631 implementation should be more technically optimized through the combination of the

632 radiation emulator and its infrequent use (Song and Roh, 2021), and the use of compound

633 parameterization (Song et al., 2021). In this study, the advantages of SWA with better

634 generalization are emphasized. The strengths of SWA for long-term integration can be

635 beneficial for developing a radiation emulator that can be used for seasonal prediction or

636 multi-model climate simulations that require high computational costs (e.g., O'Neill et al.,

637 2016). Furthermore, it can be also applied to improve the NN emulation studies for other

638 physical parameterizations (Brenowitz and Bretherton, 2018; Gentine et al., 2018; Rasp et al.,

639 2018; Wang et al., 2019; Chantry et al., 2021; Mooers et al., 2021). Various sensitivity

640 experiments on important hyperparameters (activation functions, hidden layers, batch sizes,

641 and learning rates) are worthwhile. These efforts will provide guidance for future

642 development toward the total replacement of numerical weather–climate forecasting models

643 using machine learning emulators.

644 **Acknowledgements**

650 **Data Availability Statement**

651 The datasets and all sources codes are available at https://doi.org/10.5281/zenodo.5638436.

652 **References**

653 Bae, S. Y., Hong, S.-Y., & Tao, W.-K. (2019). Development of a single-moment cloud
654   microphysics scheme with prognostic hail for the Weather Research and Forecasting
655   (WRF) model. *Asia-Pacific Journal of Atmospheric Sciences,* 55, 233–245.
656   https://doi.org/10.1007/s13143-018-0066-3.

657 Baek, S. (2017). A revised radiation package of G-packed McICA and two-stream
658   approximation: Performance evaluation in a global weather forecasting model. *Journal*
659   *of Advances in Modeling Earth Systems,* 9, 1628–1640.
660   https://doi.org/10.1002/2017MS000994.

661 Belochitski, A., Binev, P., DeVore, R., Fox-Rabinovitz, M., Krasnopolsky, V., & Lamby, P.
662   (2011). Tree approximation of the long wave radiation parameterization in the NCAR
663   CAM global climate model. *Journal of Computational and Applied Mathematics*, 236,
664   447–460. https://doi.org/10.1016/j.cam.2011.07.013.

665 Belochitski, A., & Krasnopolsky, V. (2021). Robustness of neural network emulations of
666   radiative transfer parameterizations in a state-of-the-art General Circulation Model.
667   *Geoscientific Model Development, Discussions,* https://doi.org/10.5194/gmd-2021-114
668   (in press).

669 Bottou, L. (2012). Stochastic Gradient Descent tricks. *Neural Networks: Tricks of the Trade.*
670   *Lecture Notes in Computer Science*, 7700. Springer, Berlin, Heidelberg.
671   https://doi.org/10.1007/978-3-642-35289-8_25.

672 Brenowitz, N. D., & Bretherton, C. S. (2018). Prognostic validation of a neural network
673   unified physics parameterization. *Geophysical Research Letters,* 45, 6289–6298.
674   https://doi.org/10.1029/2018GL078510.

675 Chantry, M., Hatfield, S., Dueben, P., Polichtchouk, I., & Palmer, T. (2021). Machine
676   learning emulation of gravity wave drag in numerical weather forecasting. *Journal of*
677   *Advances in Modeling Earth Systems*, *13*, e2021MS002477.
678   https://doi.org/10.1029/2021MS002477.

Chevallier, F., Chéruy. F., Scott, N. A., & Chédin, A. (1998). A neural network approach for a fast and accurate computation of a longwave radiative budget. *Journal of Applied Meteorology,* 37, 1385–1397. https://doi.org/10.1175/1520-0450(1998)037.

Chevallier, F., Morcrette, J.-J., Chéruy, F., & Scott, N. A. (2000). Use of a neural-network-based long-wave radiative-transfer scheme in the ECMWF atmospheric model. *Quaterly Journal of the Royal Meteorological Society,* 126, 761–776. https://doi.org/10.1002/qj.49712656318.

Clough, S. A., Iacono, M. J., & Moncet, J.-L. (1992). Line-by-line calculation of atmospheric fluxes and cooling rates: Application to water vapor. *Journal of Geophysical Research,* 97, 15761–15785. https://doi.org/10.1029/92JD01419.

Clough, S. A., Shephard, M. W., Mlawer, E. J., Delamere, J. S., Iacono, M. J., Cady-Pereira, K., Boukabara, S., & Brown, P. D. (2005). Atmospheric radiative transfer modeling: a summary of the AER codes. *Journal of Quantitative Spectroscopy and Radiative Transfer,* 91, 233–244. https://doi.org/10.1016/j.jqsrt.2004.05.058.

Gentine, P., Pritchard, M., Rasp, S., Reinaudi, G., & Yacalis, G. (2018). Could machine learning break the convection parameterization deadlock? *Geophysical Research Letters,* 45, 5742–5751. https://doi.org/10.1029/2018GL078202.

Hersbach, H., Bell, B., Berrisford, P., Hirahara, S., Horányi, A., Muñoz-Sabater, J., Nicolas, J., Peubey, C., Radu, R., Schepers, D., Simmons, A., Soci, C., Abdalla, S., Abellan, X., Balsamo, G., Bechtold, P., Biavati, G., Bidlot, J., Bonavita, M., Chiara, G., Dahlgren, P., Dee, D., Diamantakis, M., Dragani, R., Flemming, J., Forbes, R., Fuentes, M., Geer, A., Haimberger, L., Healy, S., Hogan, R. J., Hólm, E., Janisková, M., Keeley, S., Laloyaux, P., Lopez, P., Lupu, C., Radnoti, G., Rosnay, P., Rozum, I., Vamborg, F., Villaume, S., Thépaut, J.-N. (2020). The ERA5 global reanalysis. *Quarterly Journal of the Royal Meteorological Society,* 146, 1999– 2049. https://doi.org/10.1002/qj.3803.

Hertel, L., Collado, J., Sadowski, P., Ott, J., & Baldi, P. (2020). Sherpa: Robust hyperparameter optimization for machine learning. *SoftwareX,* 12, 100591, https://doi.org/10.1016/j.softx.2020.100591.

Hogan, R. J., & Bozzo, A. (2015). Mitigating errors in surface temperature forecasts using approximate radiation updates. *Journal of Advances in Modeling Earth Systems*, 7, 836–853. https://doi.org/10.1002/2015MS000455.

Iacono, M. J., Delamere, J. S., Mlawer, E. J., Shephard, M. W., Clough, S. A., & Collins, W. D. (2008). Radiative forcing by long-lived greenhouse gases: Calculations with the AER radiative transfer models. *Journal of Geophysical Research,* 113, D13103. https://doi.org/10.1029/2008JD009944.

Izmailov, P. Podoprikhin, D., Garipov, T., Vetrov, D., and Wilson, A. G. (2018). Averaging weights leads to wider optima and better generalization. *Conference on Uncertainty in Artificial Intelligence (UAI) 2018,* https://arxiv.org/abs/1803.05407.

Jiménez, P. A., Dudhia, J., González-Rouco, J. F., Navarro, J., Montávez, J. P., García-Bustamante, E. (2012). A revised scheme for the WRF surface layer formulation. *Monthly Weather Review*, 140, 898–918. https://doi.org/10.1175/MWR-D-11-00056.1.

Krasnopolsky, V. M., Fox-Rabinovitz, M. S., & Chalikov, D. V. (2005). New approach to calculation of atmospheric model physics: Accurate and fast neural network emulation of longwave radiation in a climate model. *Monthly Weather Review*, 133, 1370–1383. https://doi.org/10.1175/MWR2923.1.

Krasnopolsky, V. M., Fox-Rabinovitz, M. S., Tolman, H. L., & Belochitski, A. A. (2008). Neural network approach for robust and fast calculation of physical processes in numerical environmental models: Compound parameterization with a quality control of larger errors. *Neural Networks,* 21, 535–543. https://doi.org/10.1016/j.neunet.2007.12.019.

Krasnopolsky, V. M., Fox-Rabinovitz, M. S., Hou, Y. T., Lord, S. J., & Belochitski, A. A. (2010). Accurate and fast neural network emulations of model radiation for the NCEP coupled Climate Forecast System: Climate simulations and seasonal predictions. *Monthly Weather Review*, 138, 1822–1842. https://doi.org/10.1175/2009MWR3149.1

Krasnopolsky, V. M. (2014). NCEP neural network training and validation system: Brief description of NN background and training software. Environment Modeling Center, NCEP/NWS, NOAA. https://doi.org/10.7289/v5qr4v2z.

Kwon, Y. C., & Hong, S. (2017). A mass-flux cumulus parameterization scheme across gray-zone resolutions. *Monthly Weather Review*, 145, 583–598. https://doi.org/10.1175/MWR-D-16-0034.1.

Li, M., Zhang, T., Chen, Y., and Smola, A. J. (2014). Efficient mini-batch training for stochastic optimization. *Proceedings of the 20th ACM SIGKDD international conference on knowledge discovery and data mining,* 661–670, https://doi.org/10.1145/2623330.2623612.

Liu, Y., Caballero, R., & Monteiro, J. M. (2020). RadNet 1.0: exploring deep learning architectures for longwave radiative transfer. *Geoscientific Model Development*, 13, 4399–4412. https://doi.org/10.5194/gmd-13-4399-2020.

Manners, J., Thelen, J.-C., Petch, J., Hill, P., & Edwards, J. M. (2009). Two fast radiative transfer methods to improve the temporal sampling of clouds numerical weather prediction and climate models. *Quaterly Journal of the Royal Meteorological Society,* 135, 457–468. https://doi.org/10.1002/qj.385.

Mandt, S., Hoffman, M. D., & Blei, D. M. (2017). *Journal of Machine Learning Research,* 18, 1–35. https://www.jmlr.org/papers/volume18/17-214/17-214.pdf.

Meyer, D., Hogan, R. J, Dueben, P. D, & Mason, S. L. (2021). Machine learning emulation of 3D cloud radiative effects. *Journal of Advances in Modeling Earth Systems,* https://arxiv.org/abs/2103.11919. (in revision)

Mooers, G., Pritchard, M., Beucler, T., Ott, J., Yacalis, G., Baldi, P., & Gentine, P. (2021). Assessing the potential of deep learning for emulating cloud superparameterization in climate models with real-geography boundary conditions. *Journal of Advances in Modeling Earth Systems*, 13, e2020MS002385. https://doi.org/10.1029/2020MS002385

O'Neill, B. C., Tebaldi, C., van Vuuren, D. P., Eyring, V., Friedlingstein, P., Hurtt, G., Knutti, R., Kriegler, E., Lamarque, J.-F., Lowe, J., Meehl, G. A., Moss, R., Riahi, K., &

Sanderson, B. M. (2016). The Scenario Model Intercomparison Project (ScenarioMIP) for CMIP6. *Geoscientific Model Development,* 9, 3461–3482. https://doi.org/10.5194/gmd-9-3461-2016.

Pal, A., Mahajan, S., & Norman, M. R. (2019), Using deep neural networks as cost-effective surrogate models for Super-Parameterized E3SM radiative transfer. *Geophysical Research Letters,* 46, 6069–6079. https://doi.org/10.1029/2018GL081646.

Pauluis, O., & Emanuel, K. (2004). Numerical instability resulting from infrequent calculation of radiative heating, *Monthly Weather Review,* 132, 673–686. https://doi.org/10.1175/1520-0493(2004)132.

Pincus, R., & Stevens, B. (2013). Paths to accuracy for radiation parameterizations in atmospheric models. *Journal of Advances in Modeling Earth Systems,* 5, 255–233. https://doi.org/10.1002/jame.20027.

Pincus, R., Mlawer, E. J., & Delamere, J. S. (2019). Balancing accuracy, efficiency, and flexibility in radiation calculations for dynamical models. *Journal of Advances in Modeling Earth Systems,* 11, 3087–3089. https://doi.org/10.1029/2019MS001621.

Roh, S., & Song, H.-J. (2020). Evaluation of neural network emulations for radiation parameterization in cloud resolving model. *Geophysical Research Letters,* 47, e2020GL089444. https://doi.org/10.1029/2020GL089444.

Shin, H. H., & Hong, S. (2015). Representation of the subgrid-scale turbulent transport in convective boundary layers at gray-zone resolutions. *Monthly Weather Review*, 143, 250–271. https://doi.org/10.1175/MWR-D-14-00116.1.

Skamarock, W. C., Klemp, J. B., Dudhia, J., Gill, D. O., Liu, Z., Berner, J., Wang, W., Powers, J. G., Duda, M. G., Barker, D. M., & Huang, X.-Y. (2019). A description of the Advanced Research WRF model version 4. *NCAR Technical Notes.* https://doi.org/10.5065/1DFH-6P97.

Smith, S. L., Kindermans, P.-J., Ying, C., & Ye, Q. V. (2018). Don't decay the learning rate, increase the batch size. *6th International Conference on Learning Representations (ICLR 2018),* https://arxiv.org/abs/1711.00489.

Song, H.-J., & Roh, S. (2021). Improved weather forecasting using neural network emulation for radiation parameterization. *Journal of Advances in Modeling Earth Systems,* 13, e2021MS002609, https://doi.org/10.1029/2021MS002609.

Song, H.-J., Roh, S., & Park, H. (2021). Compound parameterization to improve the accuracy of radiation emulator in a numerical weather prediction model. *Geophysical Research Letters,* 48, e2021GL095043, https://doi.org/10.1029/2021GL095043.

Tewari, M., Chen, F., Wang, W., Dudhia, J., LeMone, M., Mitchell, K., Ek, M., Gayno, G., Weigel, J., & Cuenca, R. (2004). Implementation and verification of the unified Noah land surface model in the WRF model. *20th Conference on Weather Analysis and Forecasting/16th Conference on Numerical Weather Prediction,* American Meteorological Society, Seattle, WA, 11 – 15 Jan.

800   Ukkonen, P., Pincus, R., Hogan, R. J., Nielsen, K. P., & Kaas, E. (2020). Accelerating
801   radiation computations for dynamical models with targeted machine learning and code
802   optimization. *Journal of Advances in Modeling Earth Systems,* 12, e2020MS002226.
803   https://doi.org/10.1029/2020MS002226.

804   Vapnik, V. N. (2019). Complete statistical theory of learning. *Automation and Remote*
805   *Control,* 80, 1949–1975. https://doi.org/10.1134/S000511791911002X.

806   Veerman M. A., Pincus, R., Stoffer, R., van Leeuwen, C. M., Podareanu, D., & van
807   Heerwaarden, C. C. (2021). Predicting atmospheric optical properties for radiative
808   transfer computations using neural networks. *Philosophical Transactions of the Royal*
809   *Society A,* 379, 20200095. https://doi.org/10.1098/rsta.2020.0095.

810   Wang, J., Balaprakash, P., & Kotamarthi, R. (2019). Fast domain-aware neural network
811   emulation of a planetary boundary layer parameterization in a numerical weather
812   forecast model. *Geoscientific Model Development,* 12, 4261–4274.
813   https://doi.org/10.5194/gmd-12-4261–2019.

814 **Table 1.** List of inputs and outputs for longwave (LW) and shortwave (SW) emulators. The
815 numbers of inputs decreased by 157 and 158 for ideal and real cases under clear conditions,
816 respectively, because cloud fractions were not used.

Inputs (ideal case)	#
Pressure	1–39
Temperature	40–78
Water Vapor	79–117
Ozone	118–156
Cloud Fraction	157–186
Skin Temperature (LW)	187
Solar Constant × Cosine Zenith Angle (SW)	187
Inputs (real case)	#
Pressure	1–39
Temperature	40–78
Water Vapor	79–117
Ozone	118–156
Cloud Fraction	157–188
Skin Temperature (LW)	189
Surface Emissivity (LW)	190
Solar Constant × Cosine Zenith Angle (SW)	189
Surface albedo (SW)	190
Outputs	#
Heating Rate (LW, SW)	1–39
Upward Flux at the Top (LW, SW)	40
Upward Flux at the Bottom (LW, SW)	41
Downward Flux at the Bottom (LW, SW)	42

817

818

819   **Table 2.** Definitions of the activation functions used. All empirical coefficients were based
820   on the default settings in pytorch.

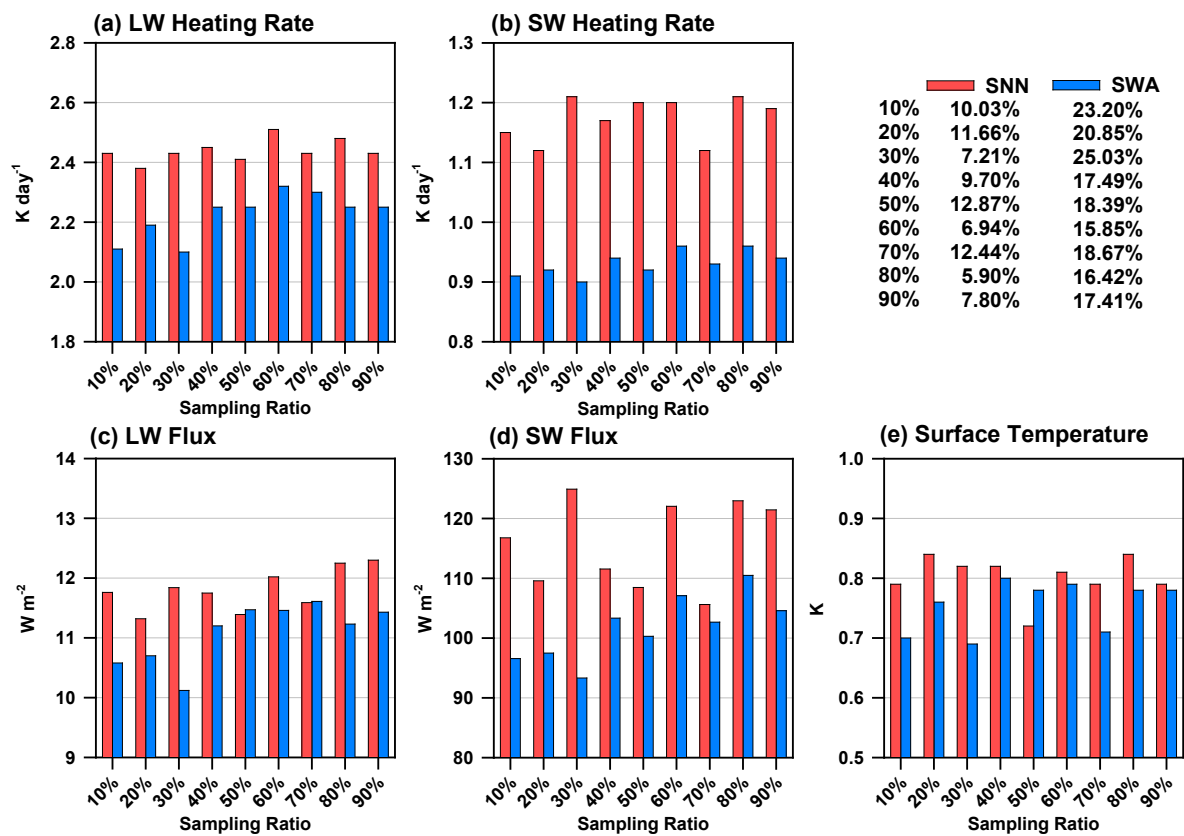| #	Functions	Equations	Ranges
1	Tanh	$(\exp(x) - \exp(-x)) \div (\exp(x) + \exp(-x))$	$-1, 1$
2	Arctan	$\tan^{-1}(x)$	$-\pi/2, \pi/2$
3	Tanhshrink	$x - \tanh(x)$	$-\infty, \infty$
4	Sigmoid	$1 \div (1+\exp(-x))$	$0, 1$
5	Logsigmoid	$\log(1 \div (1+\exp(-x)))$	$-\infty, 0$
6	SiLU	$x \div (1+\exp(-x))$	$0, \infty$
7	Softsign	$x \div (1+|x|)$	$-1, 1$
8	Softplus	$\log(1+\exp(x))$	$0, \infty$
9	Mish	$x \times \tanh(\mathrm{softplus}(x))$	$0, \infty$
10	Hardtanh	$[-1, x \leq -1], [x, -1 < x < 1], [1, x \geq 1]$	$-1, 1$
11	Hardsigmoid	$[0, x \leq -3], [x \div 6 + 1 \div 2, -3 < x < 3], [1, x \geq 3]$	$0, 1$
12	Hardswish	$[0, x \leq -3], [x \times (x+3) \div 6, -3 < x < 3], [x, x \geq 3]$	$0, \infty$
13	ReLU	$\max(0,x)$	$0, \infty$
14	LeakyReLU	$\max(0,x) + 0.01 \times \min(0,x)$	$-\infty, \infty$
15	ELU	$[x, x > 0], [\exp(x) -1, x \leq 0]$	$-1, \infty$
16	SELU	$\alpha \times (\max(0,x)+\min(0, \beta \times (\exp(x) -1)))$ $\alpha = 1.0507009873554804934193349852946$ $\beta = 1.6732632423543772848170429916717$	$-\alpha \times \beta, \infty$

821

822

823 **Table 3.** Statistical results of the idealized squalline simulation under the infrequent use of
824 radiation scheme by 9, 30, and 60 times (WRF9, WRF30, and WRF60), and the SNN/SWA
825 emulation results compared to the control run. Total improvement is the relative reduction of
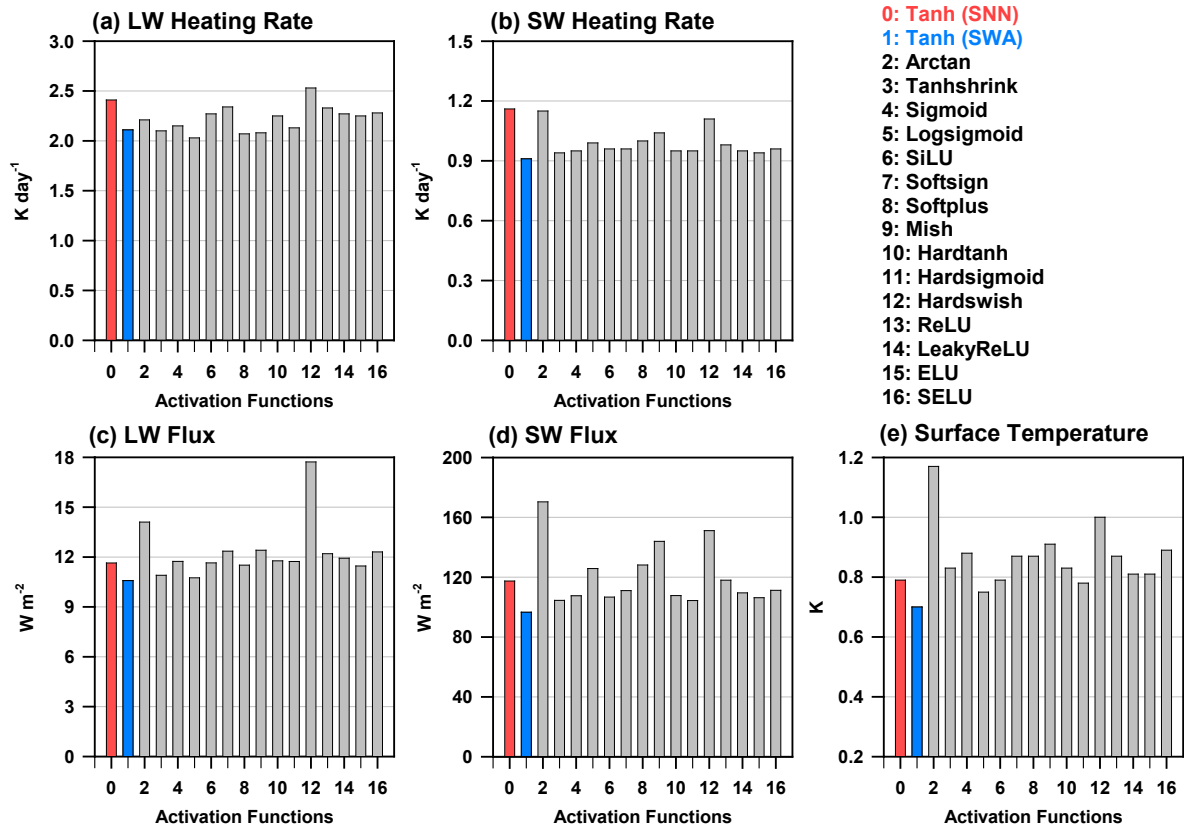826 RMSE (%) in WRF60 for five variables (LW/SW hearing rates, LW/SW flux, and surface
827 temperature).

Experiments	WRF9	WRF30	WRF60	SNN	SWA
Radiation time step (radt)	3 m	10 m	20 m	20 s	20 s
Speedup of radiation	9	30	60	59.7	60.1
Reduced total time	75.56%	82.17%	83.58%	83.61%	83.69%
LW heating rate [K day^{-1}]	2.40	2.57	2.58	2.43	2.11
SW hearing rate [K day^{-1}]	1.16	1.20	1.24	1.15	0.91
LW flux [W m^{-2}]	11.12	12.28	13.29	11.76	10.58
SW flux [W m^{-2}]	102.08	113.43	132.15	116.78	96.56
Surface temperature [K]	0.72	0.77	0.92	0.79	0.70
Total improvement (%)	14.74	8.21	-	10.03	23.20

828

829

830 **Table 4.** Root mean square error (RMSE) results of fluxes and skin temperature (T_s) in the
831 real case simulation under the infrequent use of radiation scheme by 15, 30, and 60 times
832 (WRF15, WRF30, and WRF60), the SNN, and the SWA with one to five hidden layers (1 h to
833 5 h), compared to the control run. The results of 2-m temperature (T_{2m}) and 3-h accumulated
834 precipitation were produced through comparison with surface observations in South Korea.
835 Note that the RMSE of the control run for 2-m temperature and precipitation observations
836 were 2.2581 K and 12.3526 mm, respectively.

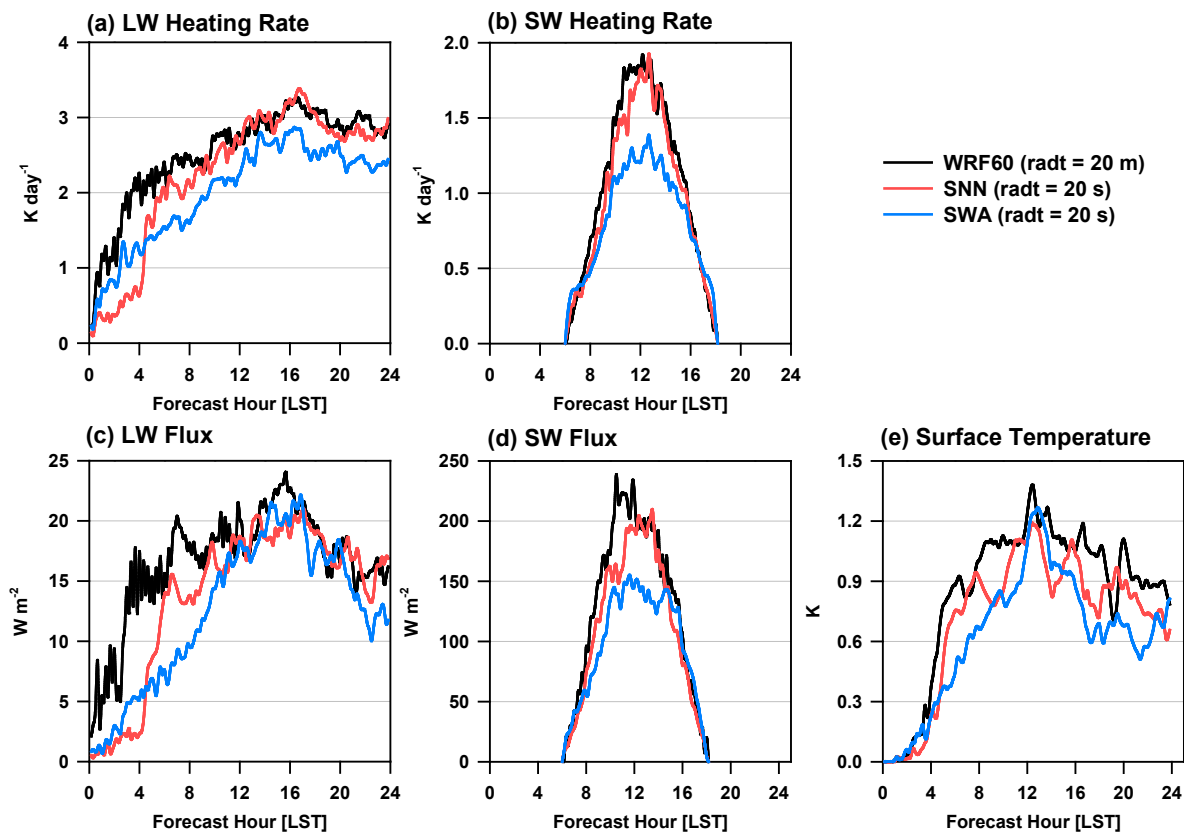| Experiments	LW flux [W m^{-2}]	SW flux [W m^{-2}]	T_s [K]	T_{2m} [K]	Precipitation [mm]
WRF15	7.8756	53.9819	0.5371	2.2590	12.2649
WRF30	8.6558	57.6258	0.5753	2.2532	12.1987
WRF60	10.1513	64.8639	0.6602	2.2438	12.2897
SNN	9.2629	61.8149	0.6721	2.2466	12.3120
SWA (1h)	8.9027	60.2215	0.6389	2.2563	12.2551
SWA (2h)	8.8680	59.6838	0.6309	2.2487	12.2944
SWA (3h)	8.9614	59.9000	0.6390	2.2470	12.3060
SWA (4h)	9.2006	60.9223	0.6563	2.2424	12.2800
SWA (5h)	9.4009	62.1192	0.6559	2.2593	12.2230

837

838

839

840

Figure 1. Sensitivity experiments with the ratio of training sets. The SNN and SWA results are represented by the ratio of training sets to full sets. Statistical values denote the RMSE using 5-km and 20-s intervals over the entire domain and period compared with the control run (radt = 20 s). Compared to the WRF60, the mean reduced RMSEs for five variables and nine ratios are presented in the upper right corner.
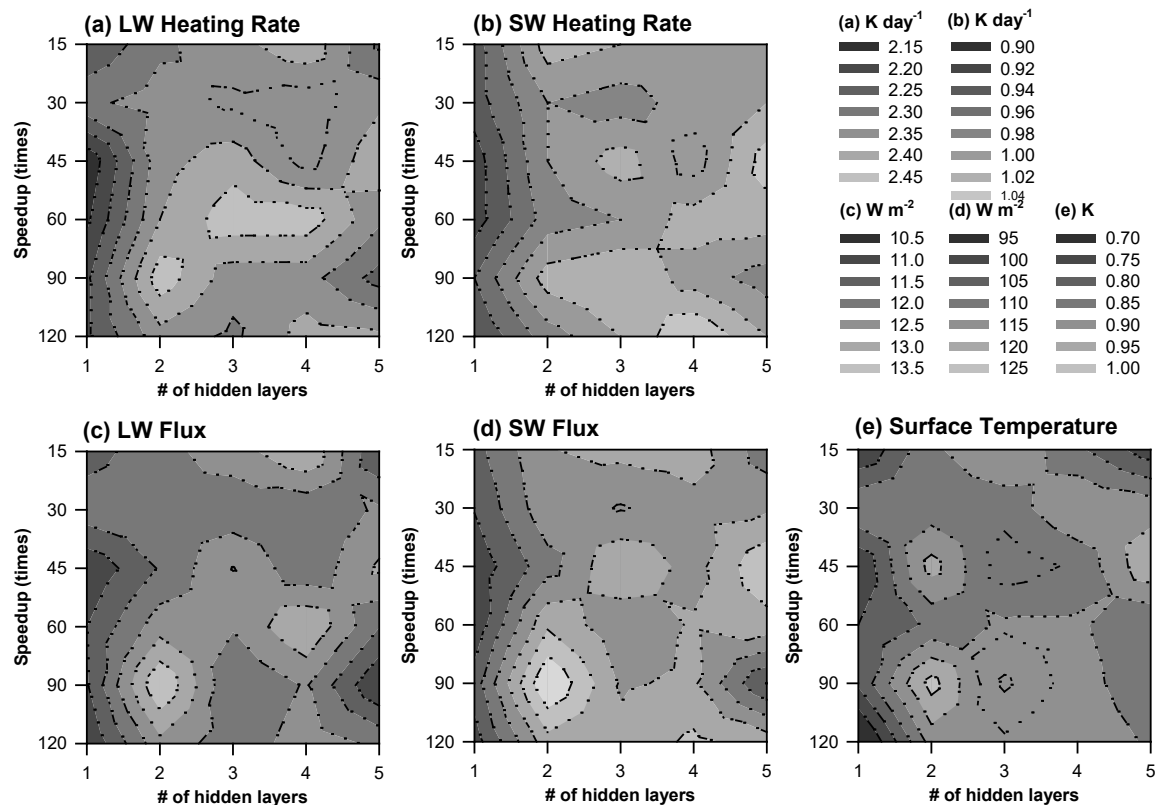
Figure 2. Sensitivity experiments with activation functions for (a) LW heating rate, (b) SW heating rate, (c) LW flux, (d) SW flux, and (e) surface temperature. Vertical bars denote the RMSE with 5-km and 20-s intervals over the entire domain and a 24-h period compared with the control run (radt = 20 s). The SNN is displayed as the red bar and the best experiment among the SWA experiments is highlighted as the blue bar.

859
860 **Figure 3.** Evolutionary features for idealized squalline simulation. The control run, WRF60
861 (radt = 20 m), SNN, and SWA results are displayed for LW and SW upward fluxes at the top
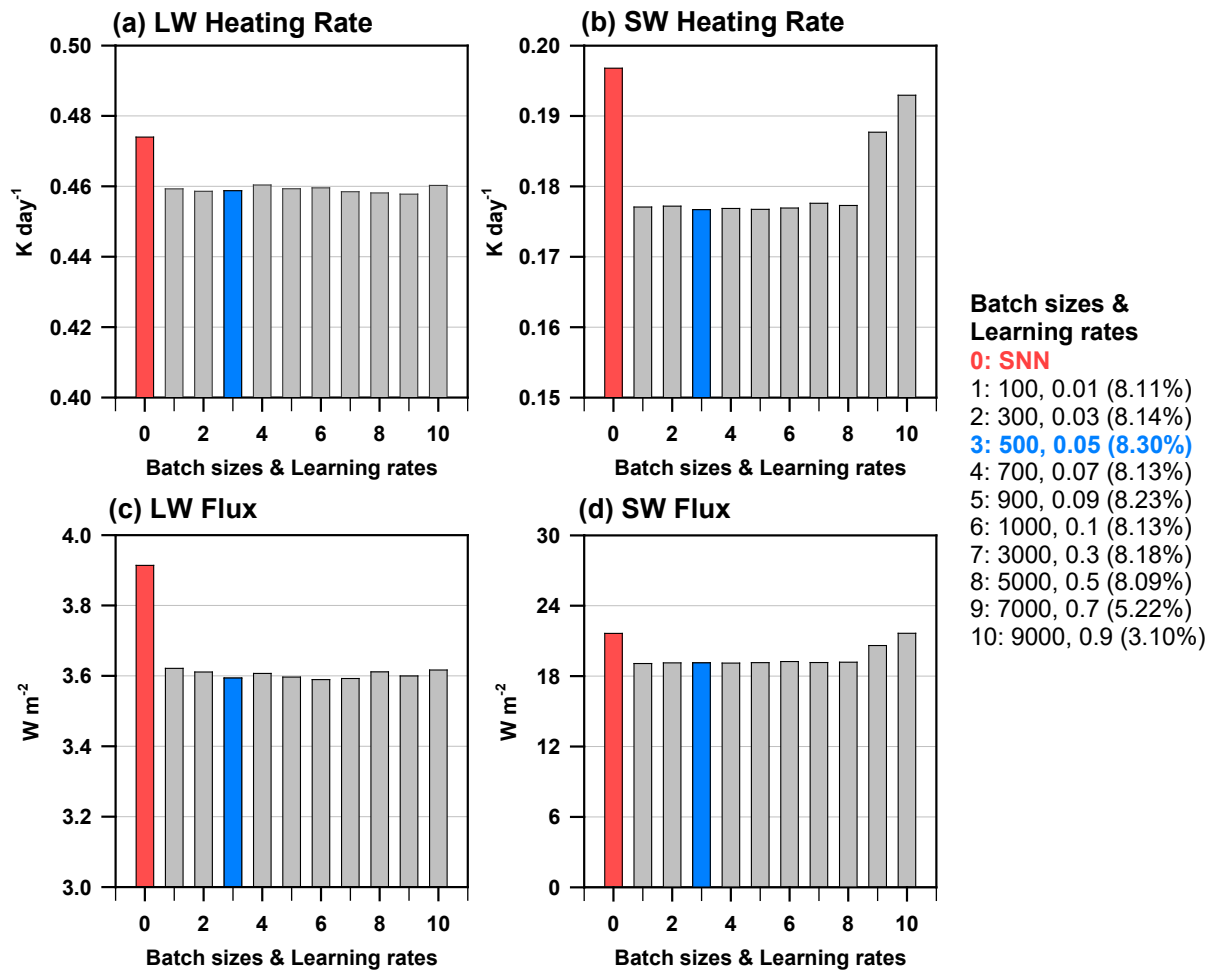862 (LWUPT and SWUPT), surface temperature, and precipitation rate.

863
864
865

Figure 4. Times series of RMSEs for (a) LW heating rate, (b) SW heating rate, (c) LW flux, (d) SW flux, and (e) surface temperature. The mean reductions in the RMSE for five variables compared to WRF60 are given in the upper right corner.
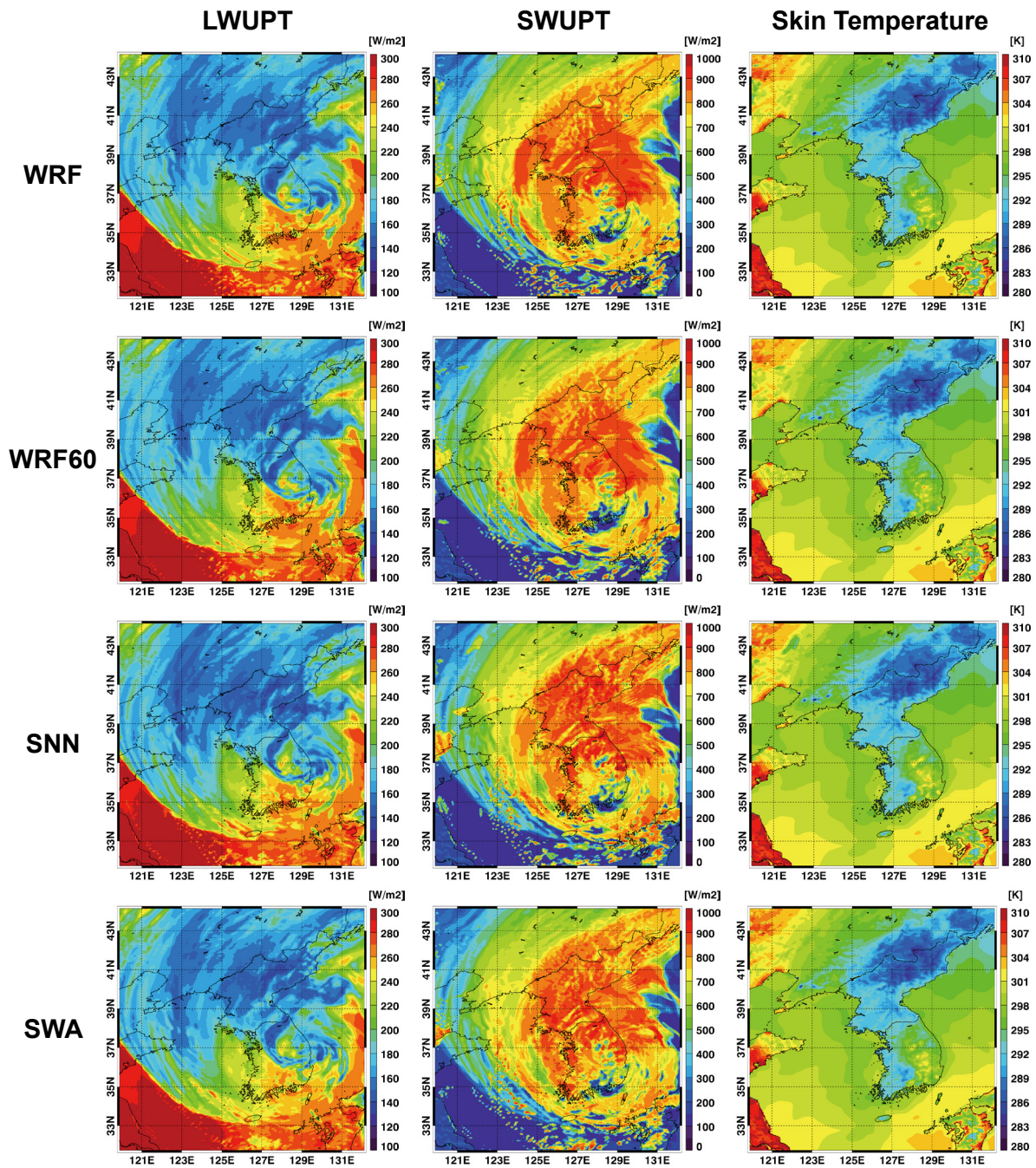
Figure 5. Sensitivity experiments with hidden layers and speedups for (a) LW heating rate, (b) SW heating rate, (c) LW flux, (d) SW flux, and (e) surface temperature. The speedups of 15, 30, 45, 60, 90, and 120 times correspond to the use of 360, 180, 120, 90, 60, and 45 neurons for the case of single hidden layer. For the case of multiple hidden layers, the reduced neurons were used to maintain the same numerical complexity and resulting speedup. The values inside each figure denote the RMSE with 5-km and 20-s intervals over the entire domain and a 24-h period compared with the control run.
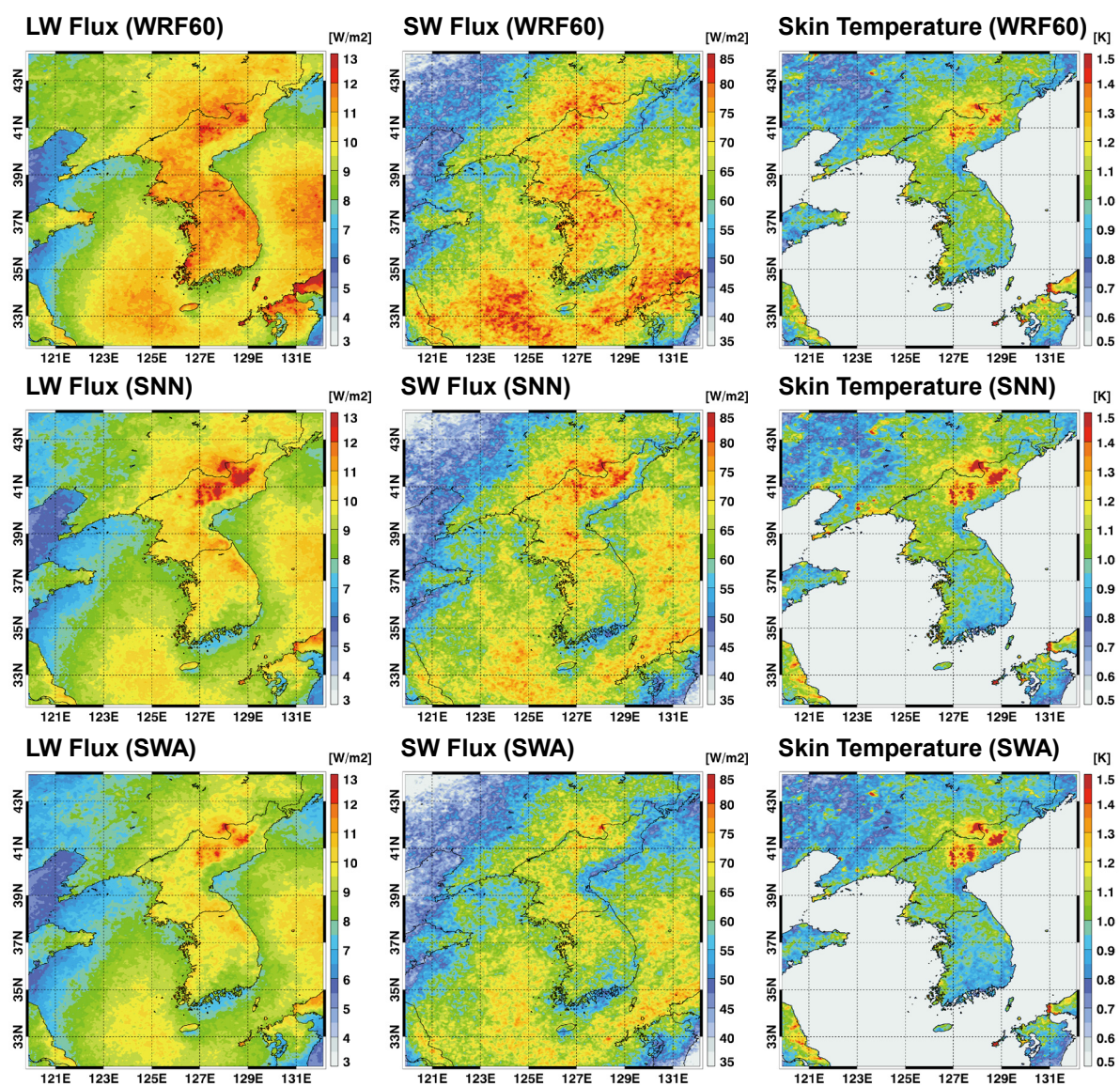
(a) LW Heating Rate

(b) SW Heating Rate

(c) LW Flux

(d) SW Flux

Batch sizes & Learning rates
0: SNN
1: 100, 0.01 (8.11%)
2: 300, 0.03 (8.14%)
3: 500, 0.05 (8.30%)
4: 700, 0.07 (8.13%)
5: 900, 0.09 (8.23%)
6: 1000, 0.1 (8.13%)
7: 3000, 0.3 (8.18%)
8: 5000, 0.5 (8.09%)
9: 7000, 0.7 (5.22%)
10: 9000, 0.9 (3.10%)

882
883 **Figure 6.** Sensitivity experiments with batch sizes and learning rates based on the SWA. The
884 RMSE values of (a) LW heating rate, (b) SW heating rate, (c) LW flux, and (d) SW flux for
885 validation sets are given in each figure. The percentages in the right corner denote the mean
886 RMSE improvements for four variables compared with SNN. This is an offline validation
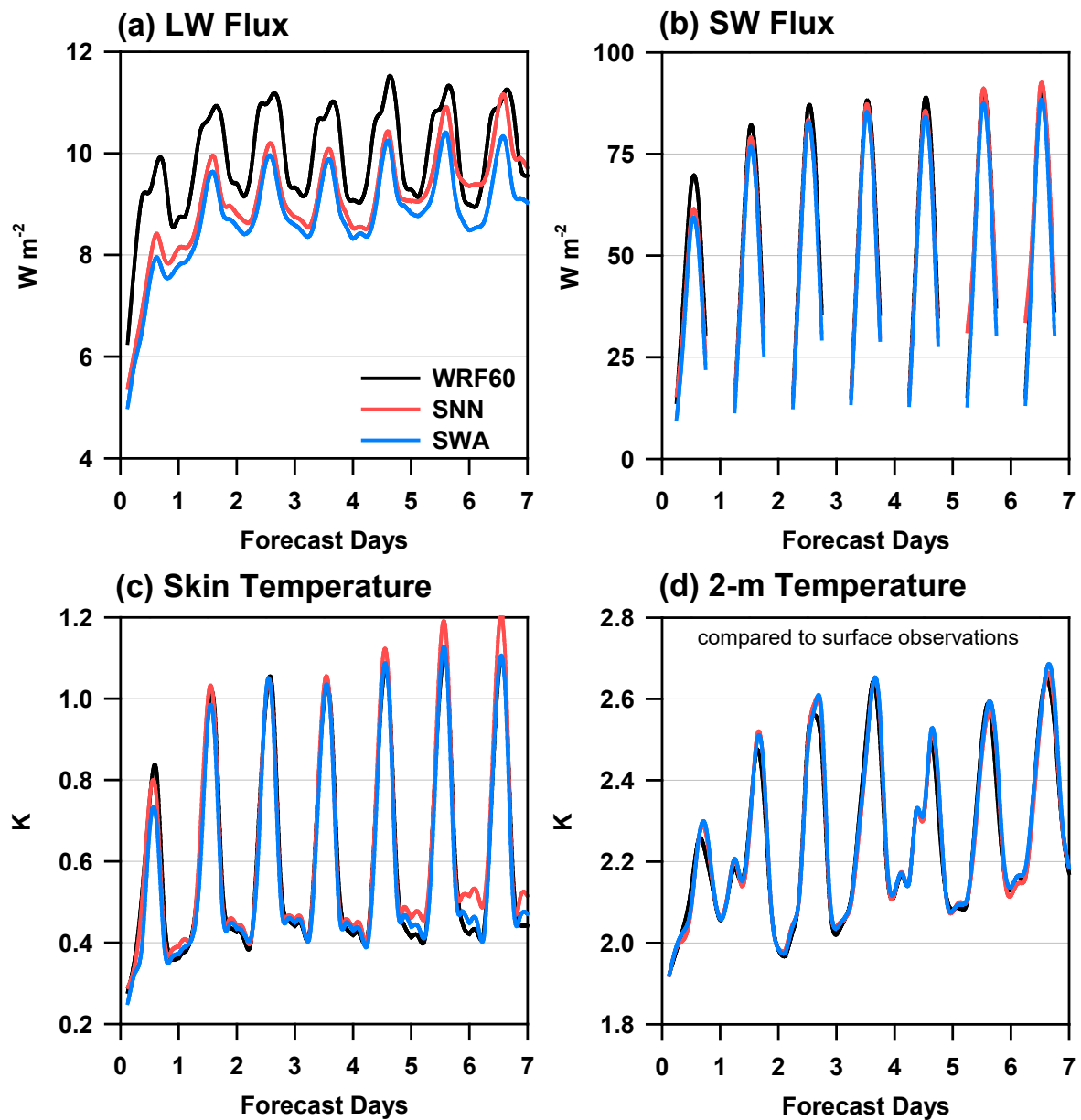887 which is not linked to the WRF simulation.

888

889

Figure 7. Example for Typhoon HAISEN (12LST September 7, 2020). Because the initial conditions started at 00LST 1 September 2020, it is 156-h forecast result. The control run, WRF60 (radt = 20 m), SNN, and SWA results are displayed for LW and SW upward fluxes at the top (LWUPT and SWUPT), and surface temperature.
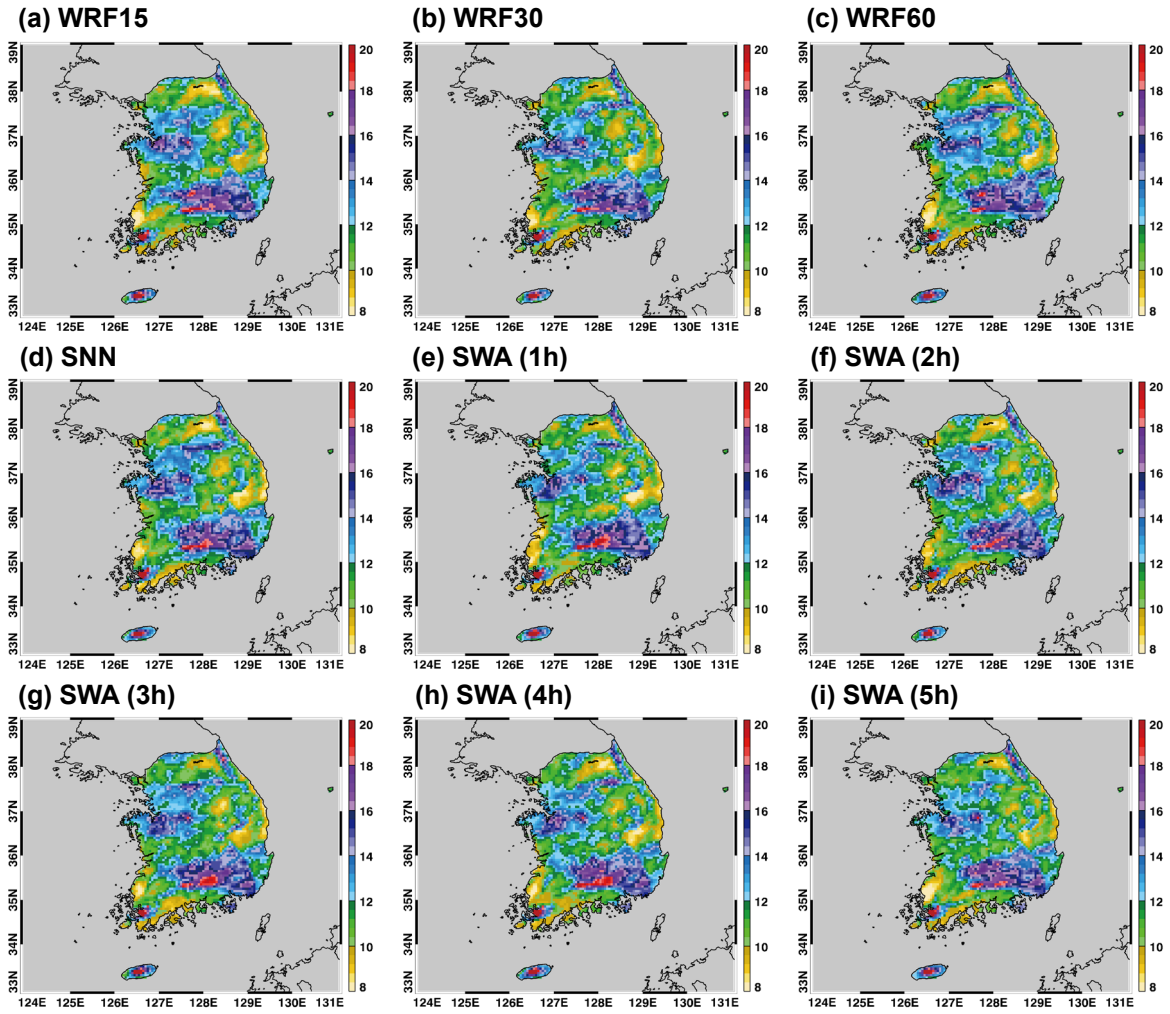
Figure 8. RMSE distributions of LW flux, SW flux, and skin temperature (T_s) for the WRF60 (radt = 20 m), SNN, and SWA compared with the control run. Each RMSE at a given 5-km grid represents a statistical result for one-week forecasts over 48 simulations of 2020.

Figure 9. Times series of RMSEs for (a) LW flux, (b) SW flux, (c) skin temperature, and (d) 2-m air temperature compared with surface observations in South Korea. The RMSE represents a statistical result over the entire domain or points (for 2-m temperature) and one-year period. The WRF60 (radt = 20 m), SNN, and SWA results are compared.

911
912 **Figure 10.** RMSE distributions of 3-h accumulated precipitation (mm) compared with the
913 observations in South Korea. The results of infrequent radiation scheme (WRF15, WRF30,
914 and WRF60), SNN, and SWA (one to five hidden layers; 1 h to 5 h) are compared.